Mapping the performance of a versatile water-based condensation particle counter (vWCPC) with COMSOL simulation and experimental study

Weixing Hao[1], Fan Mei[2,*], Susanne Hering[3], Steven Spielman[3], Beat Schmid[2], Jason Tomlinson[2], Yang Wang[1,*]

[1]Department of Chemical, Environmental and Materials Engineering,
University of Miami, Miami, FL, 33146, USA

[2]Pacific Northwest National Laboratory, Richland, WA, 99352, USA

[3]Aerosol Dynamics Inc., Berkeley, CA, 94710, USA

Correspondence to: Fan Mei (fan.mei@pnnl.gov), Yang Wang (yangwang@miami.edu)

Abstract.

Accurate airborne aerosol instrumentation is required to determine the spatial distribution of ambient aerosol particles, particularly when dealing with the complex vertical profiles and horizontal variations of atmospheric aerosols. A versatile water-based condensation particle counter (vWCPC) has been developed to provide aerosol concentration measurements under various environments with the advantage of reducing the health and safety concerns associated with using butanol or other chemicals as the working fluid. However, the airborne deployment of vWCPCs is relatively limited due to the lack of characterization of vWCPC performance at reduced pressures. Given the complex combinations of operating parameters in vWCPCs, modeling studies have advantages in mapping vWCPC performance.

In this work, we thoroughly investigated the performance of a laminar flow vWCPC using COMSOL Multiphysics® simulation coupled with MATLAB. We compared it against a modified ~~commercial~~ vWCPC (vWCPC Model 3789, TSI, Shoreview, MN, USA). Our simulation determined the performance of particle activation and droplet growth in the vWCPC growth tube, including the supersaturation, $D_{p,kel,0}$ (smallest size of particle that can be activated), $D_{p,kel,50}$ (particle size activated with 50% efficiency) profile, and final growth particle size D_d under wide operating temperatures, inlet pressures P (~~0.330~~ – 101 kPa ~~atm~~), and growth tube geometry (diameter D and initiator length L_{ini}). The effect of inlet pressure and conditioner temperature on vWCPC 3789 performance was also examined and compared with laboratory experiments. The COMSOL simulation result showed that increasing the temperature difference (ΔT) between conditioner temperature T_{con} and initiator T_{ini} will reduce $D_{p,kel,0}$ and the cut-off size $D_{p,kel,50}$ of the vWCPC. In addition, lowering the temperature midpoint ($T_{mid} = \frac{T_{con}+T_{ini}}{2}$) increases the supersaturation and slightly decreases the $D_{p,kel}$. The droplet size at the end of the growth tube is not significantly dependent on raising or lowering the temperature midpoint but significantly decreases at reduced inlet pressure, which indirectly alters the vWCPC empirical cut-off size. Our study shows that the current simulated growth tube geometry (D = 6.3 mm and L_{ini} = 30 mm) is an optimized choice for current vWCPC flow and temperature settings. The current simulation can more realistically represent the $D_{p,kel}$ for 7 nm vWCPC and also achieved a good agreement with the 2 nm setting. Using the new simulation approach, we provide an optimized operation setting for the 7 nm setting. This study will guide further vWCPC performance optimization for applications requiring precise particle detection and atmospheric aerosol monitoring.

1 Introduction

Aerosols, defined as any solid or liquid particles suspended in air, are one of the fundamental components of the atmosphere and have a significant impact on air quality, climate change and human health (Seinfeld et al., 2016; Anderson et al., 2020; Lighty et al., 2000; Pöschl, 2005; Prather et al., 2020; Li et al., 2017; Paasonen et al., 2013; Darquenne, 2012). However, accurate and comprehensive monitoring of aerosol particles is challenging because aerosol particle sizes and number concentrations vary widely both spatially and temporally (Davidson et al., 2005; Yu and Luo, 2009; Krudysz et al., 2009). Airborne measurements and characterization, therefore, are often required to capture the vertical profiles and horizontal variability of atmospheric aerosols.

In understanding the variability of atmospheric aerosol and determining the size distribution and number concentration of aerosols, laminar-flow, butanol-based Condensation Particle Counters (CPCs) used in conjunction with differential mobility analyzers (DMAs) can provide real-time measurements of airborne particles and are widely used by effectively exploiting the working principle of condensation growth (Ahn et al., 1990, Ahn et al., 1990; Hermann et al., 2007; Kangasluoma and Attoui, 2019; Mordas et al., 2008; Sem, 2002; Wiedensohlet et al., 1997). However, conventional butanol CPCs face difficulties in characterizing particles below 3 nm in size. In addition, health and safety risks, such as the odor, flammability and toxicity of the butanol, are an issue for many deployments in offices, homes, aircraft, and other inhabited locations. These limitations have led directly to researchers designing advanced aerosol instruments that can be more widely used in both atmospheric environments and laboratory studies.

In 2005, Hering and Stolzenburg (2005) developed a continuous-flow, water-based laminar condensation particle counter (WCPC) (Hering et al., 2005; Hering and Stolzenburg, 2005), which uses distilled water as the working fluid to avoid the health and safety concerns. It was also found to have comparable performance to butanol-based CPCs in previous studies (Biswas et al., 2005; Franklin et al., 2010; Iida et al., 2008; Kupc et al., 2013; Liu et al., 2006; Mordas et al., 2008). A modified version of the WCPC featuring an additional new moderator section has been developed (Hering et al., 2014). With this new moderated approach, the initiator provides water vapor for particle activation while the moderator provides distance and time for particle growth. This improved water CPC achieves the same peak supersaturation and similar droplet growth while reducing the water vapor, particle loss, and side effects of heating the flow in the earlier version of WCPC. Furthermore, a versatile WCPC was then developed capable of particle detection near 1 nm without using a filtered sheath flow. The operating temperatures can also be adjusted in accordance with the cut-point desired (Hering et al., 2017).

75

Since water-based CPCs have comparable performance to butanol-based CPCs while also offering the advantage of avoiding health and safety risks, it is desirable to explore advanced water-based CPCs in a broader range of environmental and energy applications. To improve the detection performance of the vWCPC, we need to identify the effects of operational factors and geometry. However, the limited analysis of relevant temperature and geometric parameters in the vWCPC makes it challenging to control condensational growth conditions. In addition, the inlet pressure effect is another critical factor affecting the detection efficiency of vWCPCs. The potential of using vWCPC for airborne deployment or other lower pressure monitoring has not been fully explored. Mei et al. (2021) found that the counting efficiency of the vWCPC 3789 operated at the factory settings decreased with decreasing the operating pressure, particularly at operating pressures below 700 hPa. However, determining how to reduce the lower detection limit under various ambient pressures also needs to be investigated.

Due to the complex matrix of geometry, operating temperature, and inlet pressure parameters in vWCPCs, modeling studies are advantageous in determining and optimizing the detection efficiency of vWCPCs. The Graetz model was first used by Stolzenburg (1988) to examine the detection of ultrafine particles in CPCs. In recent years, COMSOL Multiphysics® has been widely used to simulate coupled heat, mass, and momentum transfer problems associated with complex geometries in CPCs. Moreover, COMSOL has advantages in interfacing with post-processing software such as MATLAB^{TM}. A series of parametric analyses for butanol CPCs were simulated using COMSOL to investigate the performance of particle activation and droplet growth (Hao et al., 2021; Attoui, 2018; Kangasluoma et al., 2015; Barmpounis et al., 2018; Thomas et al., 2018). Our previous work (Hao et al., 2021) first demonstrated that the COMSOL results neglecting the temperature dependence of vapor thermodynamic properties and axial diffusion, agree with the Graetz solution used by Stolzenburg (1988). Considering temperature dependence of vapor thermodynamic properties and axial diffusion can generate more accurate results that can guide the optimization of CPC designs. Previous research using COMSOL to examine vWCPC performance has been limited. Bian et al. (2020) compared two-stage and three-stage operating temperature methods for growth tubes and parameters such as flow rate and temperature difference to obtain the ideal activation and final growth sizes. Mei et al. (2021) used COMSOL aiding to examine how inlet pressure affects particle activation in the vWCPCs. However, the lack of thorough and systematic examination of vWCPC performance using COMSOL leaves it unclear on how well the vWCPC will perform in multiple complex research areas and applications, such as at reduced atmospheric pressure levels.

106   In this study, we thoroughly determined the saturation profile, activation efficiency, and droplet growth for
107 varying airborne operations through numerical simulation of laminar flow vWCPC in COMSOL and experimental
108 validation of a commercial vWCPC (TSI Model 3789). By mapping vWCPC performance in the modeling, the
109 effects of various operational factors, such as inlet pressures (~~0.3~~30 - 101 ~~atm~~kPa), growth tube diameter and
110 initiator length, and temperature gradients on particle activation and droplet growth, were investigated. In addition,
111 detailed modeling methods are outlined below. The detection efficiency was also examined in the experimental
112 and COMSOL modeling work. The results of this study will guide further optimization of the performance of
113 vWCPCs for accurate detection of particles and atmospheric aerosol measurement applications.
114
115 **2 Methods**
116 **2.1 Numerical simulation**
117 **2.1.1 COMSOL setup**
118   The finite element COMSOL simulation software (COMSOL Multiphysics 5.3a, COMSOL Inc, Stockholm,
119 Sweden) can handle a variety of fields including, but not limited to, electromagnetics, fluid dynamics, heat
120 transfer, chemical reactions, and structural mechanics. Here, a two-dimensional axisymmetric model is developed
121 to simulate fluid flow in a cylindrical tube. The heat, momentum, and mass transfer equations are solved for
122 incompressible parabolic flow. This COMSOL model follows the three-stage tube of the versatile water-based
123 CPC (TSI Inc, Shoreview, MN, USA) described by Hering et al. (2017), which consists of a fully developed
124 laminar flow tube that can be separated into a cool-wall conditioner region, a warm-wall initiator region, and a
125 cool-wall moderator region, where r is the radial coordinate of the tube diameter and z is the axial coordinate of
126 the tube length (**Fig. 1a**). At the inlet of the conditioner tube, sampled aerosols are fed and saturated with water
127 vapor before entering the initiator region. The manufacturer provides two default cut-off diameter settings: 2 and
128 7 nm configurations based on the characteristics introduced by Kangasluoma et al. (2017). This study used the 7
129 nm configuration as an example to demonstrate the simulation mapping effort. The methodology can also be used
130 for other targeted cut-off sizes. The tube diameter (D) is 6.3 mm, the conditioner length (L_{con}) is 73 mm, the
131 initiator length (L_{ini}) is 30 mm, and the moderator length (L_{mod}) is 73 mm. The default settings are (**Table 1**): the
132 conditioner temperature (T_{con}) is 30 °C, the initiator temperature (T_{ini}) is 59 °C, and the moderator temperature
133 (T_{mod}) is 10 °C. The aerosol flow rate (Q_v) is 0.3 L min^{-1}. The relative humidity (RH) of inlet flow is set at 20%,
134 and the water vapor is assumed to be saturated at the wall. The inlet pressure (P) is ~~1 atm~~101 kPa. To investigate
135 how the vWCPC performance depends on these parameters, we simulate a wide range of values for mapping the

136 vWCPC geometry, working temperature conditions, and inlet pressure, as discussed in Section 2.1.4 for the tasks
137 in this study.

138

139 In this COMSOL model, the coupled heat transfer and fluid flow are first solved by the conjugate heat transfer
140 module, and then the mass transfer of the water vapor is solved based on the obtained temperature and flow field.
141 Lastly, the particles are introduced from the inlet of the vWCPC and are considered diluted species that follow
142 the convective diffusion equation in the simulation, which is numerically solved to calculate the temperature,
143 supersaturation, and water vapor concentration profiles (**Fig. 1**). Regarding the initial and boundary value settings,
144 the inflow temperature is set to an ambient temperature of 25 °C, and wall temperature is set to the default factory
145 settings described above and changed as the experimental conditions changed for mapping performance. The
146 simulated temperature and concentration fields are then imported into MATLAB™ R2022b (The MathWorks,
147 Inc., Natick, MA, USA) and interpolated at any given point in the *r-z* plane. COMSOL Multiphysics 5.3a with
148 MATLAB allows us to adjust geometry, modify physics settings, perform parametric studies, control solvers, and
149 post-process the results.

150

151 **2.1.2 Theory of particle activation**

152 Particle activation is key to the evaluation of CPC performance. Particle activation within the vWCPC depends
153 on the degree of supersaturation, namely the saturation ratio (S) of water vapor, which is the ratio of the partial
154 pressure of the water vapor (p) to the saturation vapor pressure of the water vapor (p_s) for the given flow
155 temperature (T), calculated by

$$S = \frac{p}{p_s} \qquad\qquad (1)$$

156 The spatial profile of S within the vWCPC allows us to calculate the Kelvin effect, the homogeneous nucleation,
157 and further condensational particle growth, as discussed in Section 2.1.3. The Kelvin effect is dependent upon
158 thermodynamic principles and described as the Kelvin equivalent size ($D_{p,kel}$), the minimum diameter of a particle
159 that can be activated for condensation growth. It is determined by water surface tension (σ), water molecular
160 volume (v_m), the Boltzmann constant (k), temperature (T) and the saturation ratio (S) calculated at each location
161 within the initiator,

$$D_{p,kel} = \frac{4\sigma v_m}{kT ln(S)} \qquad\qquad (2)$$

162 The Kelvin equivalent size is inversely proportional to the distribution of saturation ratio, where the greater the

163 saturation ratio, the smaller the size of the particles that can be activated. In other words, the smaller the particle,

164 the higher the degree of supersaturation required to activate growth. When particle size (D_p) is above $D_{p,kel}$, the

165 particle can be successfully activated and grown by water vapor condensation, while when D_p is below $D_{p,kel}$, the

166 particles cannot be activated. **Fig. 1b - 1e** show examples of saturation ratio, Kelvin equivalent size, water vapor

167 concentration, and temperature profiles within the simulated geometry at the default temperature condition of T_{con}

168 = 30 °C, T_{ini} = 59 °C, T_{mod} = 10 °C, respectively.

169

170 It is worth noting that $D_{p,kel}$ varies at different locations of the initiator due to the spatial variation of temperature,

171 surface tension and saturation ratio. We observed the potential particle activation in the moderator by simulation

172 results. However, only the Kelvin equivalent size in the initiator was considered in this work. Although the

173 particles were activated in the moderator, particle detection was unlikely due to droplet growth being the dominant

174 water vapor sink in the initiator. Thus, in reality, the actual supersaturation in the moderator may be different, and

175 the activation of smaller particles will be hindered by droplet growth (Hering et al., 2014; Hering et al., 2017).

176 Note that the $D_{p,kel}$ in the conditioner region is blank in color due to no particles being activated in this region (S

177 $\leqslant$1).   Particles near the wall of the initiator, where there is a lower S, are more difficult to activate due to the

178 larger $D_{p,kel}$. This difference can be explained by the water mass and heat diffusivity differences. As the colder,

179 water-saturated flow passes through the growth tube, the mass transport of water vapor is faster than the heating

180 of the flow from the wall because the mass diffusivity of water vapor is higher than the thermal diffusivity of air,

181 producing a maximum supersaturation of water vapor at the centerline of the tube. As a result, the seed particles

182 entering near the centerline of the growth tube are activated in the warmer initiator. One comparison of the

183 saturation ratio and Kelvin equivalent size along the centerline (r = 0) is shown in **Fig. S1a and S1b.** We observed

184 the appearance of a double-peaked saturation ratio curve. Again, only the Kelvin equivalent size in the initiator

185 was considered in this work due to insufficient water vapor and droplet growth in the moderator. Note that the

186 solute effect is negligible under the water-based condensation particle growth and is not included in the following

187 simulation. As shown in **Fig. S2**, around 1% variation was observed in the final droplet size by adding the solute

188 effect into the droplet growth simulation. ~~Note that our calculations do not include the solute effects, and we~~

189 ~~assume wettable insoluble particles in the modeling.~~

190

191   The activation efficiency of particles with a size of D_p in vWCPC is derived using an approach similar to our

192   previous work (Hao et al., 2021), which is calculated by the ratio of the number concentration of the activated

193   particles over the total particle number concentration in the growth tube. The activation efficiency is calculated as

$$\eta_{\text{act}} = \frac{\int_0^{R_{\text{act}}} 2\pi r w N dr}{Q_v N_0} \tag{3}$$

194   where w is the velocity along the axial direction, N is the concentration of particles, both at the axial location of

195      $z = Z_{\text{act}}$. R_{act} is the maximum radius of the contour corresponding to $D_{p,\text{kel}} = D_p$. N_0 is the particle concentration

196   at the inlet of the conditioner. Q_v is the flow rate through the vWCPC. An example of activation efficiency as a

197   function of particle diameter D_p can be found in **Fig. S1c**. Note that the calculation of the activation efficiency in

198   Eq. (3) does not consider the diffusion loss of the particles in the conditioner. Since this model does not have

199   sheath flow that minimizes the diffusion losses and constrains the aerosols to the high supersaturation region, the

200   activation efficiency cannot reach 100%. On the activation curve, there are two points of interest: minimum

201   activated size, $D_{p,\text{kel},0}$ (the smallest size of particle that can be activated in the initiator), and 50% cut-off

202   size, $D_{p,\text{kel},50}$ (the size of a particle with 50% activation efficiency extracted from the activation efficiency curve).

203      $D_{p,\text{kel},50}$ is essential to the performance of CPCs because it determines the general particle size range in which

204   the CPC can confidently measure. $D_{p,\text{kel},50}$ can be used as the representative of particle activation efficiency

205   performance. Furthermore, note that negligible homogeneous nucleation occurs in the growth tube of the initiator

206   and moderator under all tested conditions in this study, which means the total nucleation rate is equal to or less

207   than one particle per second (1 s^{-1}).

208

2.1.3 Theory of droplet growth

210   Once the particles are activated, their condensational growth along their trajectories in the initiator region was

211   simulated by numerically solving two coupled differential equations in MATLAB™. First, the evolution of

212   droplet diameter (D_p) can be ~~governed~~ estimated by (Seinfeld and Pandis, 2008; Wang et al., 2017)

$$\frac{dD_p}{dt} = \frac{4 D_v' M}{\rho} \frac{(C - C_d)}{D_p} \tag{5}$$

213   where M and ρ represent the molecular weight and density of water, D_v' represents the modified diffusivity of the

214   water vapor accounting for the non-continuum effect of the particles and is given by $D_v' = D_v \left[1 + \right.$

215    $\frac{2D_v}{\alpha_c D_p}(\frac{2\pi M}{RT})^{1/2}\Big]^{-1}$, where D_v is the diffusivity of the water vapor, and α_c is the mass accommodation coefficient of

216   water and is assumed as 1. C_d represents the equilibrium water concentration at the surface of the growth droplets

217   and is given by $C_d = C_s(T_d)exp\left(\frac{4\sigma M}{\rho R T_d D_p}\right)$, where C_s is saturation water concentration, T_d is the droplet surface

218   temperature, which is governed by

$$\frac{dT_d}{dt} = \frac{3}{c_p \rho D_p}\left(H_{vap}\rho\frac{dD_p}{dt} - 4k'_g\frac{(T_d - T)}{D_p}\right) \tag{6}$$

219   where c_p, ρ, and H_{vap} are the heat capacity, density, and heat of vaporization of water. k'_g represents the modified

220   thermal conductivity of air accounting for the non-continuum effects in heat transfer and is calculated as $k'_g =$

221    $k_g\left[1 + \frac{2k_g}{\alpha_T D_p \rho_g c_{p,g}}\left(\frac{2\pi M_g}{RT}\right)^{1/2}\right]^{-1}$, where M_g, ρ_g, $c_{p,g}$, and k_g are the molecular weight, density, heat capacity, and

222   thermal conductivity of air. α_T is the thermal accommodation coefficient and was assumed to be 1 (Seinfeld and

223   Pandis, 2008; Wang et al., 2017).

224

225   In the simulation of droplet growth, the Brownian motion of the particles inside the conditioner before activation

226   is neglected. Since there is also no electric field inside the conditioner, we assume that the particles move axially

227   along the vWCPC with a velocity of w. Therefore, Eqs. (5) and (6) can be converted to a function of axial location

228   using $w = dz/dt$, and the droplet size and droplet surface temperature at the end of the moderator ($z = L_{ini} +$

229   L_{mod}) can be calculated. To determine the final droplet growth size at the outlet of the moderator, the

230   condensational growth of 8 nm particles as seed particles was studied along the centerline ($r = 0$) of the growth

231   tube in this work. An example of droplet growth size as a function of distance along the axis of the tube for the

232   default temperature condition of $T_{con} = 30$ °C, $T_{ini} = 59$ °C, $T_{mod} = 10$ °C can be found in **Fig. S1d**. Note that in

233   this simulation, we do not consider the increase in the equilibrium vapor pressure due to warming of the flow from

234   condensational heat release, which would further reduce the droplet growth.

235

236   **2.1.4 Simulation plan**

237   **Table 1** summarizes the operating temperatures, inlet pressures, and geometric parameters for each simulation

238   task characterizing the vWCPC in this study. In Task 1, we first conducted two matrix combinations of absolute

239   conditioner and initiator operating temperatures, with an interval of 5 °C in each region, for a total of nine different

240   combinations. Task 2 investigates how raising or lowering the temperature midpoints (T_{mid}), the average value

241 between the conditioner temperature and initiator temperature ($\frac{T_{con}+T_{ini}}{2}$) affects particle activation and droplet

242 growth. In addition, different inlet pressures are also included when comparing different temperature midpoints.

243 Task 3 examines the effect of inlet pressure ~~by comparing~~at the default conditioner temperature of 30 ℃ and the

244 customized conditioner ~~conditioner~~ temperature of 27 ℃. Tasks 4 and 5 further test how the vWCPC geometry,

245 including tube diameter D, and initiator length L_{ini}, affects the performance of the vWCPC. These simulations

246 reveal optimal working conditions and effects for the influence of each parameter.

247

248 **2.2 Experimental measurement**

249 The modified vWCPC 3789 (TSI Inc, Shoreview, MN, USA) was tested in this study. Given that the standard

250 commercially available vWCPC 3789 is not specifically designed for low-pressure applications, some

251 modifications were made to the instrument for this study. First, the vWCPC 3789 was tested to ensure its vacuum

252 tightness~~,. As a result, the make-up air flow port and exhaust port were blocked during the vacuum-tight check~~

253 ~~and the exhaust line was filtered and returned back to the make-up flow line after a flow buffer. Second, the~~

254 ~~vWCPC 3789 monitors inlet pressure, orifice pressure, and nozzle pressure during operation. Therefore, we~~

255 ~~connected the ambient and inlet pressure ports to the low-pressure manifold to prevent triggering of the warning~~

256 ~~and error indicators. Third,~~ we added pressure transducers to the inlet and exhaust lines of the vWCPC 3789 to

257 monitor the inline pressure variation. ~~Finally, when we operated with 1.5 L min⁻¹ inlet aerosol flow, we blocked~~

258 ~~the make-up flow port.~~ Note that the aerosol flow rate through the condenser tube and optical particle detector

259 was 0.3 L min^{-1}. When we operated with 0.6 L min^{-1} inlet aerosol flow, we blocked the make-up flow port. Details

260 of o~~O~~perating flow, temperatures and geometry ~~can be found~~are provided in Section 2.1.1 ~~and~~. Further specifics

261 can be found in our previous study (Mei et al., 2021).

262

263 Two methods were used to generate the test aerosol: an atomizer coupled with a furnace; and a glowing wire

264 generator (GWG). Ammonium sulfate (AS) has been commonly used for CPC characterization and was the tested

265 material used in this study (Hering et al., 2014; Kangasluoma et al., 2017). It was dissolved into deionized water

266 for aerosol generation using atomization techniques. To increase the aerosol number concentration for particles

267 less than 30 nm, polydisperse AS aerosols were also passed through a tube furnace generator at the temperature

268 of 500 ℃ and flow rate of 1.5 lpm (Lindberg/Blue, Thermal Scientific, TX, USA) to shift the size distribution to

269 a smaller size. A lab-built GWG was also used to generate aerosol particles in size range between 2.5 – 16 nm.

270 More details about the generator can be found in Attoui (2022). Using the low-pressure testing setup shown in

271 **Fig. S2**, the counting efficiency of a vWCPC 3789 was measured between 0.551 -and 0.991 kPa atm for AS

272 particles of 3 – 20 nm (mobility diameter) and NiCr oxidants of 2.5 -16 nm. The aerosol concentrations in this

273 test were maintained in the range of $2\times10^4 – 4\times10^4$ cm^{-3}. During the testing, the temperature variations in the

274 conditioner and moderator were less than 0.5 ℃, and the initiator temperature had a variation of 1 ℃. The y-axis

275 error bar indicates the standard deviation of the counting efficiency averaged over ~ 5 min of sampling time at a

276 1 Hz sampling rate.

277

278 **3 Results and discussion**

279 **3.1 Comparisons of temperature-dependent particle activation and droplet growth performance**

280 Selection of appropriate operating temperatures in CPCs is essential because the supersaturation is significantly

281 temperature dependent, which affects particle activation and further droplet growth. In addition, the temperature

282 difference between different regions in CPCs is an important factor in controlling supersaturation. For this reason,

283 the minimum activation size for butanol-based CPCs is significantly impacted by the temperature difference

284 between the saturator and condenser and the raising or lowering of the temperature midpoints, as has been

285 demonstrated by many previous studies (Hermann and Wiedensohler, 2001; Kangasluoma and Attoui, 2019;

286 Barmpounis et al., 2018; Kuang et al., 2012). The results showed that in the butanol-based CPCs, the greater the

287 temperature difference between the saturator and condenser, the higher the degree of supersaturation, and the

288 smaller particle could be activated.

289

290 The numerical COMSOL model was used to compare operating temperature-dependent particle activation and

291 droplet growth performance in the vWCPC, including minimum activated size ($D_{p,kel,0}$), 50% cut-off size

292 ($D_{p,kel,50}$), and final growth particle size at the outlet of the moderator along the centerline ($r = 0$) (D_d), as shown

293 in **Fig. 23**. Previous studies confirmed that the centerline saturation rate is insensitive to the moderator wall

294 temperature (Hering et al., 2014; Bian et al., 2020). Thus, this study investigated moderator temperature (T_{mod})

295 at the constant of 10 ℃, conditioner temperature (T_{con}) at the range of 25 – 35 ℃, initiator temperature (T_{ini}) at

296 the range of 55 – 65 ℃. Note that conditions that can lead to a lower $D_{p,kel,50}$ value and larger droplet growth size

297 are favored for improving the performance of the vWCPC.

298

Firstly, in order to compare the effect of the conditioner temperature T_{con}, we ~~increased~~ varied T_{con} from 25 ℃ to 35 ℃ while maintaining the same initiator temperature T_{ini} and moderator temperature T_{mod}. The results show that, $D_{p,kel,0}$ increased significantly by 5.21, 3.32, and 2.27 nm at the initiator temperature T_{ini} of 55, 60, and 65 ℃, respectively, and $D_{p,kel,50}$ increased significantly by 6.65, 4.16, and 2.75 nm at the initiator temperature T_{ini} of 55, 60, and 65 ℃, respectively. The final droplet size D_d decreased by approximately 1 μm at all the initiator temperature T_{ini} of 55, 60, 65 ℃. The lower conditioner temperature provided higher saturation ratios in the initiator and more water vapor for particle growth, which is also consistent with the previous growth tube simulation (Bian et al., 2020; Mei et al., 2021). Secondly, the initiator temperature T_{ini} was increased from 55 ℃ to 65 ℃ while maintaining the same conditioner temperature T_{con} and moderator temperature T_{mod}, $D_{p,kel,0}$ was decreased by 1.90, 3.74, and 4.87 nm at the conditioner temperature T_{con} of 25, 30, and 35 ℃, respectively, $D_{p,kel,50}$ was decreased significantly by 2.32, 3.74, and 6.21 nm at the conditioner temperature T_{con} of 25, 30, and 35 ℃, respectively, and D_d was increased by 2.9 μm at all the conditioner temperature T_{con} of 25, 30, and 35 ℃.

By comparing all combinations, we can find that the activated size becomes smaller as the temperature difference between T_{con} and T_{ini} increases, indicating that the temperature differences between the conditioner and initiator dominate the particle activation. After comparing the temperature differences, we conclude that the higher the temperature between these two regions, the better the particle activation. However, in the actual operation of the CPC, one also needs to ensure that the self-nucleation in the growth tube is minimized (<1 s^{-1}) so that the CPC does not report false particle counting. The homogeneous nucleation rate is less than 10^{-8} s^{-1} at all tested conditions, meaning that the temperatures can be further adjusted to optimize particle activation and droplet growth. Moreover, D_d is the greatest, with a maximum size of 12.20 μm, at the temperature setting of 25–65–10 ℃ among all these temperature conditions. We also found that the effect of the initiator temperature on droplet growth was greater than that of the conditioner temperature. Thus, the following section examines the effect of temperature midpoint on the vWCPC performance.

3.2 Effect of temperature midpoint on particle activation and droplet growth performance

In addition to temperature difference, lowering the temperature midpoint was also found to cause higher supersaturation. However, there is limited research on how the performance of the vWCPC changes under various temperature midpoints and especially under different inlet pressures, which will be important for applications such

328   as atmospheric airborne deployment and environmental monitoring at elevated locations. Here, we compared the

329   particle activation and droplet growth performance for three different temperature midpoints (40 °C, 43 °C, and

330   46 °C) of conditioner temperature (from 24 °C to 30 °C) and initiator temperature (56 °C to 62 °C) at a wide range

331   of inlet pressures from ~~0.3~~30 ~~atm~~ kPa to 1~~01~~ ~~atm~~kPa, as shown in **Fig. 3**4. The temperature difference ΔT between

332   the conditioner and the initiator was kept constant at 32 °C. The moderator temperature remained constant at 10

333   °C in all simulations.

334

335   Results show that the minimum activated size $D_{p,kel,0}$ decreases from 5.15 nm to 4.96 nm, and the 50% cut-off

336   size $D_{p,kel,50}$ decreases from 5.88 nm to 5.65 nm as the temperature midpoint decreases from 46 °C to 40 °C, as

337   shown in **Fig. 3a**4a **and** 3b4b. Thus, a slight control of the minimum activation size can be achieved by lowering

338   the temperature midpoint. Higher supersaturation can explain this slight decrease in the initiator, which also agrees

339   with the previous growth tube WCPC simulation (Bian et al., 2020). On the other hand, a slight increase of 0.07,

340   0.1, and 0.14 nm occurs in $D_{p,kel,0}$, and negligible change in $D_{p,kel,50}$ by reducing the inlet pressure from 101 to

341   0.3~~30 kPa atm~~ under three temperature midpoints of 40 °C, 43 °C, and 46 °C. This slight increase is due to a low

342   peak supersaturation caused by the decrease in inlet pressure. Since water vapor transport is faster than heat

343   transport, the decrease in pressure affects the location of the peak supersaturation, whereas the degree of the

344   supersaturation does not change significantly.

345

346   In **Fig. 3c**4c, we show that the droplet growth is not significantly dependent on raising or lowering the temperature

347   midpoint. By lowering the temperature midpoint by 6 °C, D_d becomes smaller by approximately 14%. When

348   studying the effect of inlet pressure on the D_d, unlike $D_{p,kel,0}$ and $D_{p,kel,50}$, D_d decreases substantially from 101

349   to 30 kPa~~1 to 0.3 atm~~, by approximately 45%. Limited by the optical chamber design of the commercial vWCPC,

350   the droplets smaller than 8 μm may not gain sufficient pulse signal to get counted. Thus, when operating under

351   lower inlet pressure, the apparent cut-off size of vWCPC may increase and needs to be further determined. The

352   reduced pressure strongly affects the final droplet growth size, likely due to the faster water vapor and heat

353   transport at reduced pressure. The thermal and mass diffusivity is inversely proportional to the pressure in the

354   growth tube, resulting in insufficient time for droplet growth. In addition, we found that with the lower inlet

355   pressure, the final droplet size reduced more notably. For example, D_d decreased from 10.6 to 10.4 μm (by 0.2

356   μm) as pressure reduced from 10.0~~1~~ to 0.9~~91 kPa~~ ~~atm~~, while D_d decreased from 7.2 to 6.1 μm (by 1.1 μm) as

357   pressure reduced from 0.4~~41~~ to 0.3~~30~~ ~~atm~~kPa. The difference can be explained by the competition between heat

358   and water vapor transport. The mass transport of water vapor is faster than the ~~heating~~ heat flow from the wall

359   because the mass diffusivity of water vapor is higher than the thermal diffusivity of air. Therefore, by reducing

360   the inlet pressure, water vapor transport becomes even faster than heat transfer due to the water vapor diffusivity

361   and air thermal diffusivity being inversely proportional to the pressure, further shortening the time for particle

362   growth at high supersaturation. This observation demonstrates for the first time how the final droplet size is

363   affected by raising or lowering temperature midpoints at standard and various reduced inlet pressure conditions

364   in the vWCPC.

365

366   **3.3 Effect of inlet operation pressure on particle activation and droplet growth performance**

367   With the advantages of safe, eco-friendly and readily available distilled water as working fluid in the vWCPC,

368   applying the vWCPC in various inlet pressures will expand broader applications such as atmospheric airborne

369   aerosol measurements. Here, we examined the effect of inlet pressure on minimum activated size, $D_{p,kel,0}$, 50%

370   cut-off size, $D_{p,kel,50}$, and final growth particle size at the outlet of the moderator along the centerline ($r = 0$), D_d

371   from ~~0.3~~30 to 1~~01~~ kPa ~~atm~~ for two different temperature settings: the conditioner, initiator, and moderator

372   temperatures were 30, 59, and 10 °C and 27, 59, and 10 °C in **Fig. 4~~5~~**.

373

374   **Figs. ~~4a~~ 5a and ~~4b~~ 5b** show $D_{p,kel,0}$ and $D_{p,kel,50}$ as a function of inlet pressure, relatively greater (2 - 3%) $D_{p,kel,0}$

375   was observed at reduced inlet pressures at both conditioner temperatures of 27 °C and 30 °C. This increase is

376   because the supersaturation value at reduced pressure is lower than the saturation profile under standard

377   conditions. We also found that the saturation profile peaked earlier, closer to the entrance of the initiator in the

378   low-pressure condition. In addition, greater $D_{p,kel,50}$ is observed at reduced inlet pressures due to the reduction of

379   the saturation peak at both conditioner temperatures of 27 °C and 30 °C. Again, the difference at reduced inlet

380   pressure can be explained by the competition from heat transfer and water vapor transport, as discussed in Section

381   3.2. For this reason, greater $D_{p,kel,50}$ was observed at reduced inlet pressures. This reduction of saturation peaks

382   is also associated with the growing droplet size decreasing with the decrease in the operating pressure. Again,

383   lowering the conditioner temperature while maintaining the same temperature difference between the initiator and

384   the moderator provided higher saturation ratios in the initiator over all pressure ranges.

385

386   **Fig. ~~4c~~ 5c** shows the final droplet size as a function of inlet pressure. When the conditioner temperature is 27 or

387   30 °C, a lower final droplet size (~ 40 % reduction in the droplet size) was observed at a reduced inlet pressure of

388 ~~0.3 atm~~30 kPa, indicating insufficient droplet growth happens at low-pressure conditions, which is consistent with

389 the previous study that insufficient droplet growth becomes more significant under low-pressure operation (Mei

390 et al., 2021).

391

392 Furthermore, in addition to showing consistent results with the previous study (Mei et al., 2021), our simulations

393 enhance guidance for aircraft applications under extreme conditions, which can be achieved by simulating low

394 atmospheric pressure at 30 kPa~~0.3 atm~~. As shown in Section 3.5, by comparing with experimental results, our

395 simulations can provide more accurate estimates of particle activation and droplet growth to guide vWCPC for

396 low-pressure applications.

397

398 **3.4 Effect of tube diameter and initiator length on particle activation and droplet growth performance**

399 The geometry in CPCs also impacts the CPC activation performance and particle growth due to the changed

400 supersaturation and temperature profile in the tube, as discussed in previous studies (Hao et al., 2021; Hering et

401 al., 2014). Here, we examined how the tube diameter D and the length of initiator L_{ini} in the vWCPC may affect

402 the minimum activated size, $D_{p,kel,0}$, 50% cut-off size, $D_{p,kel,50}$, and final growth particle size at the outlet of the

403 moderator along the centerline ($r = 0$), D_d under default temperature $T_{con}-T_{ini}-T_{mod}$ of 30–59–10 °C, standard

404 inlet pressure and reduced pressure of 51 kPa ~~0.5 atm~~ using the numerical COMSOL model. Again, one needs to

405 note that conditions that can lead to a lower $D_{p,kel,0}$ and $D_{p,kel,50}$ value and larger droplet growth size are favored

406 for improving the performance of the vWCPC.

407

408 We examined four values of D from 4 to 8 mm, and five values of L_{ini} from 10 to 50 mm, shown in **Fig. ~~5~~6 and**

409 **Fig. ~~6~~7,** respectively. The results indicate that a smaller D can slightly decrease in $D_{p,kel,0}$ approximately 0.03 nm,

410 while no noticeable changes on $D_{p,kel,50}$ at the standard pressure (**Figs. ~~5a~~6a and ~~5b~~6b**). By reducing the tube

411 diameter, the flow speed in the tube increases under the same flow rate, reducing the residence time of the

412 condensed water vapor. This reduction in residence time suppresses homogeneous nucleation in the initiator.

413 Unlike our previous study on CPCs (Hao et al., 2021), the homogeneous nucleation rate is minimal in vWCPC

414 and has no impact on the temperature difference compared to butanol-based CPCs. For this reason, this suppressed

415 homogeneous nucleation has limited effects on $D_{p,kel,0}$ and $D_{p,kel,50}$. However, the increase of the flow speed will

416 significantly limit the time for droplet growth, as will be discussed later. At the reduced pressure of ~~0.5~~51 ~~atm~~kPa,

417 a smaller D can slightly decrease in $D_{p,kel,0}$ approximately 0.08 nm, and a slight decrease of approximately 0.03

418 nm on $D_{p,kel,50}$ (**Figs. 5a 6a and 5b6b**). Overall, the reduction in pressure plays a more critical role in negatively

419 impacting CPC performance for relatively large tube diameters. Note that buoyancy effects (Roberts and Nenes,

420 2005) may be critical for large temperature differences if the tube diameter is too large, which is not discussed in

421 the study.

422

423 On the other hand, we found that reducing L_{ini} leads to limited effects on $D_{p,kel,0}$ and $D_{p,kel,50}$, except for the

424 shortest initiator length of 10 mm at the standard pressure (**Figs. 6a 7a and 6b7b**). The effect of these relatively

425 long initiator lengths is limited because the degree of supersaturation is determined by the absolute temperature

426 of the tube flow. The temperature difference did not change in the standard pressure and reduced pressure, leaving

427 both $D_{p,kel,0}$ and $D_{p,kel,50}$ unchanged. However, at the initiator length of 10 mm, $D_{p,kel,0}$ and $D_{p,kel,50}$ increase

428 significantly due to insufficient water vapor diffusion before passing through the next moderator region, resulting

429 in a lower peak supersaturation along the centerline than for longer initiators operating at the same temperature

430 (Hering et al., 2014). At reduced pressure, $D_{p,kel,0}$ and $D_{p,kel,50}$ have no noticeable changes at all tested initiator

431 lengths, however, this is due to the sufficient diffusion of water vapor, from which the water transport is faster

432 than at the standard pressure. Again, if the initiator is longer, the difference in peak supersaturation will be

433 negligible, while the peak temperature along the centerline and the amount of added water vapor will be higher.

434 Thus, for relatively short initiators, such as 20 mm used in the simulation, one can provide all the necessary water

435 vapor to create the same peak supersaturation as for the longer initiators. However, the droplet growth size will

436 be smaller (**Fig. 6c7c**), mainly due to the shorter growth time discussed later.

437

438 With regard to the performance of particle growth, an increased D and an increased L_{ini} are beneficial for

439 improving the performance of particle growth in vWCPC at both standard and reduced pressure (**Figs. 5c 6c and**

440 **6c7c**). An increased D implies a decrease in the flow velocity through the high saturation region, greatly increasing

441 the time for particle growth and contributing to the sufficient growth of the particles. **Fig. 5c 6c** shows that the

442 final droplet sizes increase significantly from 6.72 μm to 13.88 μm when D is increased from 4 mm to 8 mm at

443 the standard pressure and increase from 4.92 to 10.78 μm at the reduced pressure of 51 kPa0.5 atm. The final

444 droplet size is found to be 2 – 3 μm smaller than the standard pressure at the reduced pressure. Similarly, a longer

445 L_{ini} also leads to a larger droplet growth size. The final droplet size increases from 8.66 μm to 11.26 μm when

446 L_{ini} is increased from 10 mm to 50 mm at the standard pressure and from 7.40 to 8.29 μm at the reduced pressure

of 51 kPa 0.5 atm (**Fig. 6c7c**). This increase is likely due to the longer growth time of the longer initiator. Also, we found that the final droplet size increases much faster at shorter initiator lengths than at lengths above 20 mm, which tells us that the droplet size is more susceptible to the effects of initiator length below 20 mm. This difference also means that having a longer length does not further enhance the final size of the particle growth.

In addition to the performance of particle activation, it is crucial to evaluate the droplet growth performance of complex geometries in the vWCPC. The time that allows the activated particle to grow in the initiator and moderator is an important droplet growth kinetics assumption, representing the vWCPC performance of droplet growth. We use t_g to represent allowed particle growth time, approximated with Eq. (7).

$$t_g \sim D^2 L^* / Q_v \tag{7}$$

where L^* indicates the length of the initiator and moderator beyond the point of activation. This equation can explain that the residence time is impacted more by the change in tube diameter than the initiator length. The allowed particle growth time as a function of final growth particle size at the outlet of the moderator along the centerline ($r = 0$), D_d is shown in **Fig. S3**. The longer the allowed particle growth time, the larger the droplet growth size. Based on this droplet growth time shown, the vWCPC geometry of D and L_{ini} are not independent variables if we consider the droplet growth for further particle detection.

3.5 Experimental measurement validation of detection efficiency

Experimental validation is essential for simulation work in terms of the accuracy of the simulation model and the correctness of the underlying trends. Furthermore, validation and good agreement will provide well-guided approaches for future applications. Therefore, we compare the experimental and simulation results of the counting efficiency and detection efficiency of vWCPC, set in two default configurations (2 nm and 7 nm) for two configurations of 2 nm and 7 nm at different conditioner and initiator temperature settings and different low-pressure conditions in **Fig. 78**.

As the experimental results in a previous study (Mei et al., 2021) are shown in **Fig. 7a8a**, the counting efficiency of vWCPC 3789 varied with different working pressures (500 1, 700 1 and 910 1 hPakPa) when the conditioner temperature is 27 °C, the initiator temperature is 59 °C, and the moderator temperature is 10 °C. The y-axis error bar indicates the standard deviation of the counting efficiency averaged over ~ 5 min of sampling time at a 1 Hz sampling rate. The results indicate that the counting efficiency slightly decreases with the decrease in the operating

476   pressure of 500**1**, 700**1** and 900**1** hPa**kPa**, which shows the same trend in **Fig. 7b8b.** In addition, the cut-off size

477   in both experimental and simulation results are in the range of 5 - 7 nm, which is also an acceptable range within

478   error when compared to commercial vWCPC detection efficiency.

479

480   **Fig. 7c 8c** and 7d **8d** compare the counting efficiency and detection efficiency versus particle size from

481   experimental and simulation results under initiator temperatures of 75 and 90°C and pressure of 910**1** and 500**1**

482   hPa **kPa** for the 2 nm configuration. As expected, the detection efficiency of both experimental and simulated

483   results is lower at the temperature $T_{con} - T_{ini} - T_{mod}$ of 7-75-10 °C at a lower pressure (at 500**1** hPa**kPa**). When the

484   temperature $T_{con} - T_{ini} - T_{mod}$ is 7-90-10 °C, the higher detection efficiency is seen, and the effect of inlet pressure

485   becomes insignificant. However, it is not feasible to maintain 90 °C when operating under lower pressure, such

486   as 500**1 kh**Pa. Thus, the default 2 nm setting in vWCPC can only be operated near sea level. One should note that

487   although we do not present many simulations for the 2 nm configuration, what we learned from the modeling

488   results with the 7 nm setting will guide future simulations with the 2 nm setting.

489

490   By comparing with counting efficiency curves, the present simulations can more realistically represent the $D_{p,kel}$

491   for 7 nm vWCPC, which also achieved a good agreement with the 2 nm setting. Thus, from the merits of the

492   results of this work, we can find that this work not only provides guidance for 7 nm, but this trend can also help

493   guide one for other desired cut-off sizes.

494

495   **4 Conclusions**

496   This study evaluated the particle activation and droplet growth performance of a commercial versatile water CPC

497   using COMSOL in combination with MATLAB data processing. In addition, validation experiments on the

498   detection efficiency of the commercially modified vWCPC (TSI 3789) agreed with the simulation work.

499   Increasing the temperature difference between T_{con} and T_{ini} and lowering the temperature midpoint can enhance

500   particle activation at both standard and reduced ambient pressure conditions. However, the lack of droplet growth

501   becomes more significant under low-pressure operations, which might affect the apparent counting efficiency of

502   the vWCPC due to the limited measurable size range of the optical chamber. Additionally, reducing the diameter

503   of the growth tube slightly improved particle activation but significantly reduced without enhancing the droplet

504   growth, while increasing the initiator length had a limited effect on improving the performance of the vWCPC at

505   both standard and reduced pressure.

506

507 This simulation realistically represents the $D_{p,kel}$ for 7 nm vWCPC and shows that the current growth tube

508 geometry is an optimized choice for aerosol measurements. This study will guide further vWCPC performance

509 optimization for applications requiring precise particle detection and atmospheric aerosol monitoring.

510 Furthermore, the developed simulation capability provides a vital tool for the aerosol community to understand

511 the effects of temperature, e and pressure, and geometry on vWCPC behavior. The knowledge gained will guide

512 the field deployment of vWCPC on the ground level and airborne measurements. However, limitations of this

513 modeling approach likely lie in the computational capacity and the difference from actual flow and temperature

514 profile distribution in the growth tube (due to non-ideal temperature control and system configuration). Thus,

515 several future experimental studies will be carried out to investigate the performance of the vWCPC.

516

517 **Data availability**

518 The vWCPC data in the study are available upon request to Fan Mei (fan.mei@pnnl.gov).

519

520 **Author contributions**

521 WH, FM, and YW designed the research. FM carried out the measurements. WH led the simulation and data

522 analyses. WH led the writing, with significant input from FM and YW as well as further input from all other

523 authors. SH, SS, BS, and JT provided suggestions on the revision.

524

525 **Competing interests**

526 Susanne Hering has a commercial interest in the success of the vWCPC instrument.

527

530

531 **References**

532 Anderson, E. L., Turnham, P., Griffin, J. R., and Clarke, C. C.: Consideration of the aerosol transmission for

533 COVID‐19 and public health, Risk Analysis, 40, 902-907, 2020. https://doi.org/10.1111/risa.13500.

Ahn, Kang-Ho and Liu, B. Y. H.: Particle activation and droplet growth processes in condensation nucleus counter--I. Theoretical background J. Aerosol Sci. 21, 249-261, 1990. https://doi.org/10.1016/0021-8502(90)90008-L.

Ahn, Kang-Ho and Liu, B. Y. H.: Particle activation and droplet growth processes in condensation nucleus counter—II. Experimental study. J. Aerosol Sci. 21, 263-275, 1990. https://doi.org/10.1016/0021-8502(90)90009-M.

Attoui, M.: Activation of sub 2 nm singly charged particles with butanol vapors in a boosted 3776 TSI CPC, J Aerosol Sci, 126, 47-57, 2018. https://doi.org/10.1016/j.jaerosci.2018.08.005.

Attoui, M.: Mobility distributions of Sub 5 nm singly self-charged water soluble and non-soluble particles from a heated NiCr wire in clean dry air, Aerosol Sci Tech, 56, 859-868, 2022. https://doi.org/10.1080/02786826.2022.2095892.

Barmpounis, K., Ranjithkumar, A., Schmidt-Ott, A., Attoui, M., and Biskos, G.: Enhancing the detection efficiency of condensation particle counters for sub-2 nm particles, J Aerosol Sci, 117, 44-53, 2018. https://doi.org/10.1016/j.jaerosci.2017.12.005.

Bian, J., Gui, H., Xie, Z., Yu, T., Wei, X., Wang, W., and Liu, J.: Simulation of three-stage operating temperature for supersaturation water-based condensational growth tube, Journal of Environmental Sciences, 90, 275-285, 2020. https://doi.org/10.1016/j.jes.2019.12.007.

Darquenne, C.: Aerosol deposition in health and disease, Journal of aerosol medicine and pulmonary drug delivery, 25, 140-147, 2012. https://doi.org/10.1089/jamp.2011.0916.

Davidson, C. I., Phalen, R. F., and Solomon, P. A.: Airborne particulate matter and human health: a review, Aerosol Sci Tech, 39, 737-749, 2005. https://doi.org/10.1080/02786820500191348.

Hao, W. X., Stolzenburg, M., Attoui, M., Zhang, J. S., and Wang, Y.: Optimizing the activation efficiency of sub-3 nm particles in a laminar flow condensation particle counter: Model simulation, J Aerosol Sci, 158, 2021. https://doi.org/10.1016/j.jaerosci.2021.105841.

Hering, S. V. and Stolzenburg, M. R.: A method for particle size amplification by water condensation in a laminar, thermally diffusive flow, Aerosol Sci Tech, 39, 428-436, 2005. https://doi.org/10.1080/027868290953416.

Hering, S. V., Spielman, S. R., and Lewis, G. S.: Moderated, water-based, condensational particle growth in a laminar flow, Aerosol Sci Tech, 48, 401-408, 2014. https://doi.org/10.1080/02786826.2014.881460.

563 Hering, S. V., Stolzenburg, M. R., Quant, F. R., Oberreit, D. R., and Keady, P. B.: A laminar-flow, water-based
564 condensation particle counter (WCPC), Aerosol Sci Tech, 39, 659-672, 2005.
565 https://doi.org/10.1080/02786820500182123.
566 Hering, S. V., Lewis, G. S., Spielman, S. R., Eiguren-Fernandez, A., Kreisberg, N. M., Kuang, C., and Attoui,
567 M.: Detection near 1-nm with a laminar-flow, water-based condensation particle counter, Aerosol Sci Tech, 51,
568 354-362, 2017. https://doi.org/10.1080/02786826.2016.1262531.
569 Hermann, M. and Wiedensohler, A.: Counting efficiency of condensation particle counters at low-pressures with
570 illustrative data from the upper troposphere, J Aerosol Sci, 32, 975-991, 2001. https://doi.org/10.1016/S0021-
571 8502(01)00037-4.
572 Hermann, M., Wehner, B., Bischof, O., Han, H.-S., Krinke, T., Liu, W., Zerrath, A., and Wiedensohler, A.:
573 Particle counting efficiencies of new TSI condensation particle counters, J Aerosol Sci, 38, 674-682, 2007.
574 https://doi.org/10.1016/j.jaerosci.2007.05.001.
575 Kangasluoma, J. and Attoui, M.: Review of sub-3 nm condensation particle counters, calibrations, and cluster
576 generation methods, Aerosol Sci Tech, 53, 1277-1310, 2019. https://doi.org/10.1080/02786826.2019.1654084.
577 Kangasluoma, J., Ahonen, L., Attoui, M., Vuollekoski, H., Kulmala, M., and Petäjä, T.: Sub-3 nm particle
578 detection with commercial TSI 3772 and Airmodus A20 fine condensation particle counters, Aerosol Sci Tech,
579 49, 674-681, 2015. https://doi.org/10.1080/02786826.2015.1058481.
580 Kangasluoma, J., Hering, S., Picard, D., Lewis, G., Enroth, J., Korhonen, F., Kulmala, M., Sellegri, K., Attoui,
581 M., and Petäjä, T.: Characterization of three new condensation particle counters for sub-3 nm particle detection
582 during the Helsinki CPC workshop: the ADI versatile water CPC, TSI 3777 nano enhancer and boosted TSI
583 3010, Atmospheric Measurement Techniques, 10, 2271-2281, 2017. https://doi.org/10.5194/amt-10-2271-2017.
584 Krudysz, M., Moore, K., Geller, M., Sioutas, C., and Froines, J.: Intra-community spatial variability of
585 particulate matter size distributions in Southern California/Los Angeles, Atmospheric Chemistry and Physics, 9,
586 1061-1075, 2009. https://doi.org/10.5194/acp-9-1061-2009.
587 Kuang, C., Chen, M., McMurry, P. H., and Wang, J.: Modification of laminar flow ultrafine condensation
588 particle counters for the enhanced detection of 1 nm condensation nuclei, Aerosol Sci Tech, 46, 309-315, 2012.
589 https://doi.org/10.1080/02786826.2011.626815.
590 Li, Z., Guo, J., Ding, A., Liao, H., Liu, J., Sun, Y., Wang, T., Xue, H., Zhang, H., and Zhu, B.: Aerosol and
591 boundary-layer interactions and impact on air quality, National Science Review, 4, 810-833, 2017.
592 https://doi.org/10.1093/nsr/nwx117.

593 Lighty, J. S., Veranth, J. M., and Sarofim, A. F.: Combustion aerosols: factors governing their size and

594 composition and implications to human health, Journal of the Air & Waste Management Association, 50, 1565-

595 1618, 2000. https://doi.org/10.1080/10473289.2000.10464197.

596 Mei, F., Spielman, S., Hering, S., Wang, J., Pekour, M. S., Lewis, G., Schmid, B., Tomlinson, J., and Havlicek,

597 M.: Simulation-aided characterization of a versatile water-based condensation particle counter for atmospheric

598 airborne research, Atmospheric Measurement Techniques, 14, 7329-7340, 2021. https://doi.org/10.5194/amt-14-

599 7329-2021.

600 Mordas, G., Petäjä, T., and Ulevičius, V.: Optimisation of the operation regimes for the water-based

601 condensation particle counter, Lithuanian Journal of Physics, 52, 2012.

602 https://doi.org/10.3952/physics.v52i3.2477.

603 Mordas, G., Manninen, H., Petäjä, T., Aalto, P., Hämeri, K., and Kulmala, M.: On operation of the ultra-fine

604 water-based CPC TSI 3786 and comparison with other TSI models (TSI 3776, TSI 3772, TSI 3025, TSI 3010,

605 TSI 3007), Aerosol Sci Tech, 42, 152-158, 2008. https://doi.org/10.1080/02786820701846252.

606 Paasonen, P., Asmi, A., Petäjä, T., Kajos, M. K., Äijälä, M., Junninen, H., Holst, T., Abbatt, J. P., Arneth, A.,

607 and Birmili, W.: Warming-induced increase in aerosol number concentration likely to moderate climate change,

608 Nature Geoscience, 6, 438-442, 2013. https://doi.org/10.1038/ngeo1800.

609 Pöschl, U.: Atmospheric aerosols: composition, transformation, climate and health effects, Angewandte Chemie

610 International Edition, 44, 7520-7540, 2005. https://doi.org/10.1002/anie.200501122.

611 Prather, K. A., Marr, L. C., Schooley, R. T., McDiarmid, M. A., Wilson, M. E., and Milton, D. K.: Airborne

612 transmission of SARS-CoV-2, Science, 370, 303-304, 2020. DOI: 10.1126/science.abc6197.

613 Roberts, G. and Nenes, A.: A continuous-flow streamwise thermal-gradient CCN chamber for atmospheric

614 measurements, Aerosol Sci Tech, 39, 206-221, 2005. https://doi.org/10.1080/027868290913988.

615 Seinfeld, J. and Pandis, S.: Atmospheric chemistry and physics. 1997, New York, 2008.

616 Seinfeld, J. H., Bretherton, C., Carslaw, K. S., Coe, H., DeMott, P. J., Dunlea, E. J., Feingold, G., Ghan, S.,

617 Guenther, A. B., and Kahn, R.: Improving our fundamental understanding of the role of aerosol− cloud

618 interactions in the climate system, Proceedings of the National Academy of Sciences, 113, 5781-5790, 2016.

619 https://doi.org/10.1073/pnas.151404311.

620 Sem, G. J.: Design and performance characteristics of three continuous-flow condensation particle counters: a

621 summary, Atmospheric research, 62, 267-294, 2002. https://doi.org/10.1016/S0169-8095(02)00014-5.

622 Stolzenburg, M. R.: An ultrafine aerosol size distribution measuring system, University of Minnesota1988.

623   Thomas, J. M., Chen, X., Maißer, A., and Hogan Jr, C. J.: Differential heat and mass transfer rate influences on

624   the activation efficiency of laminar flow condensation particle counters, International Journal of Heat and Mass

625   Transfer, 127, 740-750, 2018. https://doi.org/10.1016/j.ijheatmasstransfer.2018.07.00.

626   Wang, J., Pikridas, M., Spielman, S. R., and Pinterich, T.: A fast integrated mobility spectrometer for rapid

627   measurement of sub-micrometer aerosol size distribution, Part I: Design and model evaluation, J Aerosol Sci,

628   108, 44-55, 2017. https://doi.org/10.1016/j.jaerosci.2017.02.012.

629   Wiedensohlet, A., Orsini, D., Covert, D., Coffmann, D., Cantrell, W., Havlicek, M., Brechtel, F., Russell, L.,

630   Weber, R., and Gras, J.: Intercomparison study of the size-dependent counting efficiency of 26 condensation

631   particle counters, Aerosol Sci Tech, 27, 224-242, 1997. https://doi.org/10.1080/02786829708965469.

632   Yu, F. and Luo, G.: Simulation of particle size distribution with a global aerosol model: contribution of

633   nucleation to aerosol and CCN number concentrations, Atmospheric Chemistry and Physics, 9, 7691-7710,

634   2009. https://doi.org/10.5194/acp-9-7691-2009.

635

636

Figures and Tables of

Mapping the performance of a versatile water-based condensation particle counter (vWCPC) with COMSOL simulation and experimental study

Weixing Hao[1], Fan Mei[2,*], Susanne Hering[3], Steven Spielman[3], Beat Schmid[2], Jason Tomlinson[2], Yang Wang[1,*]

[1]Department of Chemical, Environmental and Materials Engineering,
University of Miami, Miami, FL, 33146, USA

[2]Pacific Northwest National Laboratory, Richland, WA, 99352, USA

[3]Aerosol Dynamics Inc., Berkeley, CA, 94710, USA

Correspondence to: Fan Mei (fan.mei@pnnl.gov), Yang Wang (yangwang@miami.edu)

Table of Nomenclature

c: Molecular concentration of the water vapor [mol m^{-3}]

C_d: Equilibrium water concentration at the surface of the growth droplets [mol m^{-3}]

C_s: Saturation water concentration [mol m^{-3}]

c_p: Heat capacity of the water [J K^{-1} kg^{-1}]

$c_{p,g}$: Heat capacity of air [J K^{-1} kg^{-1}]

D_v: Diffusivity of the water vapor [m^2 s^{-1}]

D'_v: Modified diffusivity of the water vapor [m^2 s^{-1}]

D: Diameter of the growth tube in vWCPC [m]

D_p: Particle size [m]

D_d: Final growth droplet size in vWCPC [m]

$D_{p,kel}$: Size of particle that can be activated according to the Kelvin equation [m]

$D_{p,kel,0}$: Smallest size of particle that can be activated in the vWCPC [m]

$D_{p,kel,50}$: Size of particle that has a 50% activation efficiency [m]

H_{vap}: Heat of vaporization of water [J kg^{-1}]

k: Boltzmann constant, 1.38×10^{-23} [J K^{-1}]

k_g: Thermal conductivity of air [W m^{-1} K^{-1}]

k'_g: Modified thermal conductivity of air [W m^{-1} K^{-1}]

L_{con}: Length of the conditioner [m]

L_{ini}: Length of the initiator [m]

L_{mod}: Length of the moderator [m]

L^*: Length of the initiator and moderator beyond the point of activation [m]

m: Molecular mass of water [kg]

M: Molecular weight of water [kg mol^{-1}]

M_g: Molecular weight of air [kg mol^{-1}]

n: Molecular concentration of the water vapor [molecules m^{-3}]

N: Concentration of the particles at the axial location of z = Z_{act} [particles m^{-3}]

N_0: Concentration of particles at the inlet of the conditioner [particles m^{-3}]

p: Partial pressure of the water vapor [Pa]

p_s: Saturation vapor pressure of the water vapor [Pa]

P: Inlet pressure in vWCPC [Pa]

Q_v: Flow rate through the vWCPC [m^3 s^{-1}]

r: Radial coordinate of the tube diameter of the vWCPC [m or as otherwise explicitly designated]

R: Gas constant [J mol^{-1} K^{-1}]

R_{act}: Maximum radius of the contour corresponding to $D_{p,kel} = D_p$ [m]

S: Saturation ratio [1]

t: Allowed particle growth time [s]

T: Flow temperature in the CPC [K]

T_{con}: Conditioner temperature [K]

T_{ini}: Initiator temperature [K]

T_{mid}: Temperature midpoint corresponding to $\frac{T_{\text{con}}+T_{\text{ini}}}{2}$ [K]

T_{mod}: Moderator temperature [K]

T_{d}: Droplet surface temperature [K]

v_{m}: Molecular volume of the water vapor [m³]

w: Velocity along the axial direction in the vWCPC [m s⁻¹]

z: Axial coordinate of the tube length of the vWCPC [m or as otherwise explicitly designated]

Z_{act}: Axial location corresponding to $r = R_{\text{act}}$ [m]

α_{c}: Mass accommodation coefficient of water [1]

α_{T}: Thermal accommodation coefficient of air [1]

η_{act}: Activation efficiency [1]

ρ: Density of water [kg m⁻³]

ρ_{g}: Density of air [kg m⁻³]

σ: Surface tension of water [N m⁻¹]

ΔT: Temperature difference between conditioner temperature and initiator temperature [K]

Table 1. Parameters of vWCPC for different simulation tasks. Note that the default settings of VWCPC are: the conditioner temperature (T_{con}) is 30 ℃, the initiator temperature (T_{ini}) is 59 ℃, and the moderator temperature (T_{mod}) is 10 ℃. The aerosol flow rate (Q_v) is 0.3 L min^{-1}. The relative humidity (RH) of inlet flow is set at 20%, and the water vapor is assumed to be saturated at the wall. The inlet pressure (P) is 101 kPa (1 atm).

Task	T_{con} (°C) - T_{ini} (°C)	T_{mod} (°C)	T_{mid} (°C)	P (kPa)	D (mm)	L_{ini} (mm)
1	(25, 30, 35) - (55, 60, 65)	10	-	101	6.3	30
2	24 - 56, 27 - 59, 30 - 62	10	40, 43, 46	30 - 101	6.3	30
3	27 - 59, 30 - 59	10	-	30 - 101	6.3	30
4	30 - 59	10	-	51, 101	4, 5, 6.3, 8	30
5	30 - 59	10	-	51, 101	6.3	10, 20, 30, 40, 50
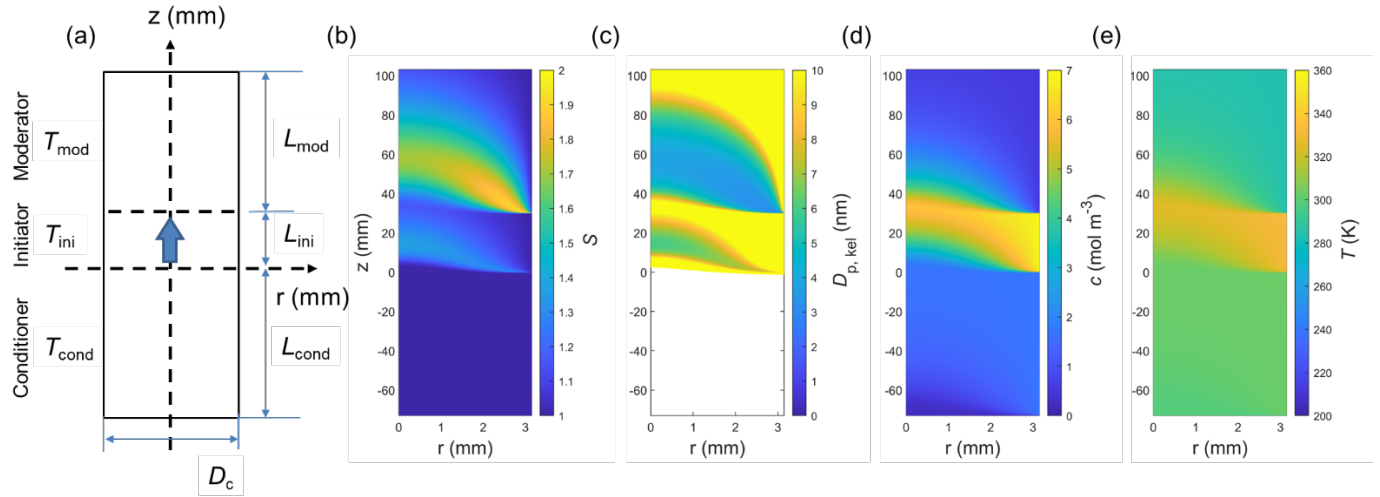
Figure 1. Geometry of vWCPC used in COMSOL simulation and spatial distribution of saturation ratio and Kelvin equivalent size under 30−59−10 °C temperature setting. (a) Geometry of the vWCPC used in COMSOL simulation, **(b)** Spatial distribution of saturation ratio (S, color contour plot), **(c)** Spatial distribution of Kelvin equivalent size ($D_{p,kel}$, color contour plot), **(d)** Spatial distribution of water vapor concentration (c, color contour plot), and **(e)** Spatial distribution of temperature (T, color contour plot). Note that the color of $D_{p,kel}$ in the conditioner region is blank because no particles are activated in this region.
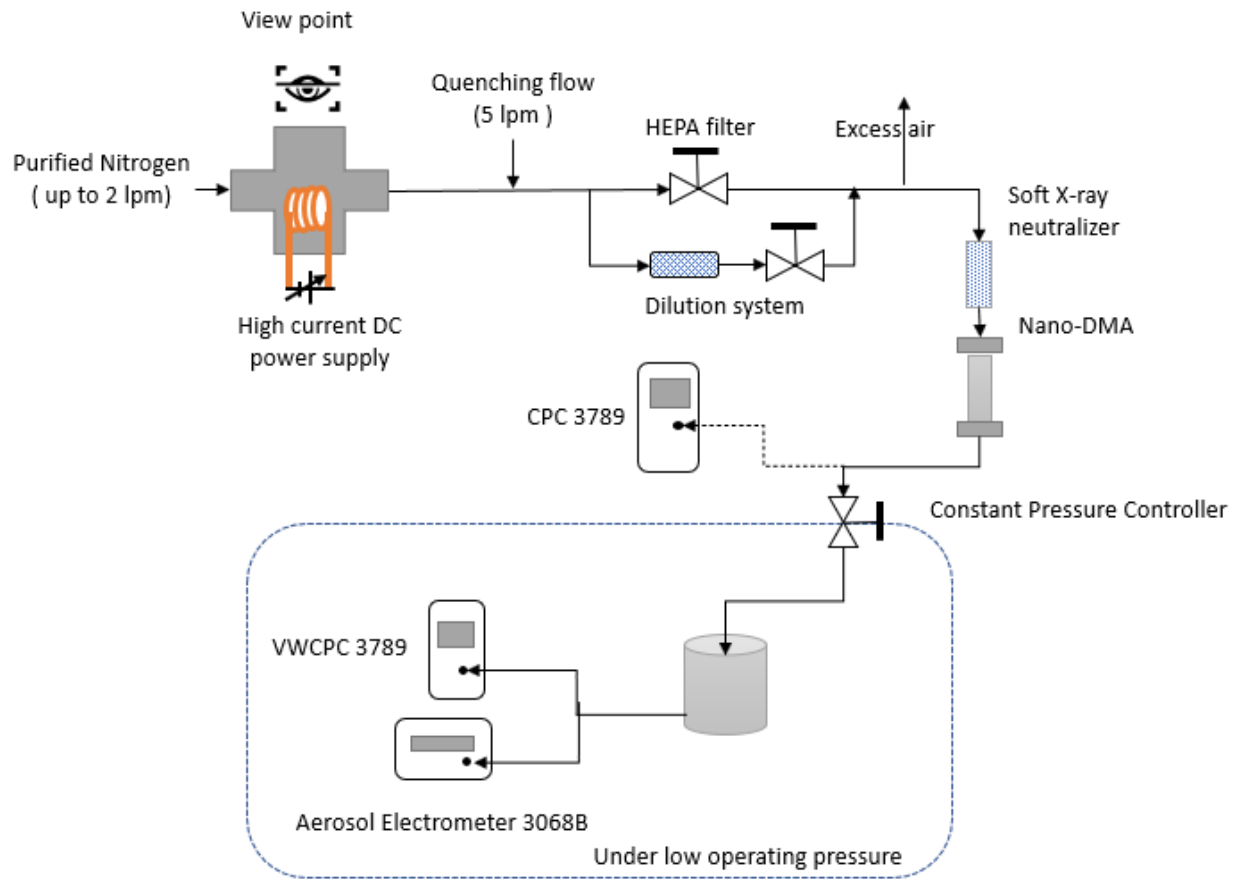
Figure. 2. Schematic diagram of the vWCPC 3789 and flow system under the low-pressure testing.
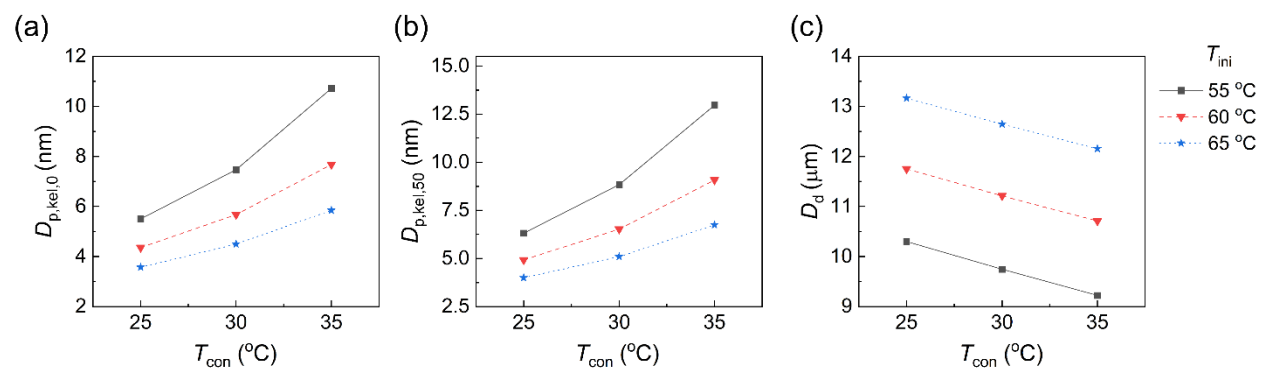
Figure 3. Effect of conditioner (T_con) and initiator temperature (T_ini) on (a) minimum activated size, $D_\text{p,kel,0}$, (b) 50% cut-off size, $D_\text{p,kel,50}$, and (c) final growth particle size at the outlet of the moderator along the centerline ($r = 0$), D_d. The condensational growth of 15 nm particles was tested as seed particles.
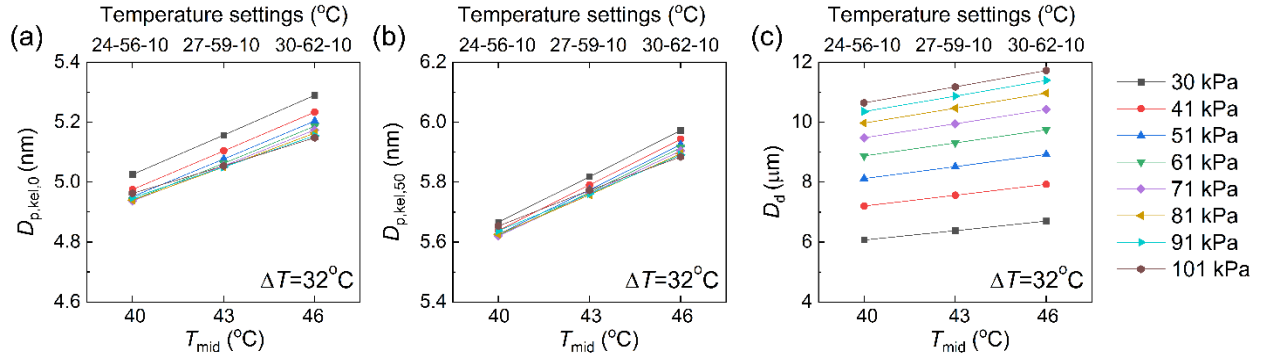
Figure 4. Effect of temperature midpoints at 40 °C, 43 °C, and 46 °C at T_{con}-T_{ini}-T_{mod} of 24–56–10 °C, 27–59–10 °C and 30–62–10 °C with a constant temperature difference of 32 °C on (a) minimum activated size, $D_{p,kel,0}$, (b) 50% cut-off size, $D_{p,kel,50}$, and (c) final growth particle size at the outlet of the moderator along the centerline ($r = 0$), D_d. The condensational growth of 8 nm particles was tested as seed particles.
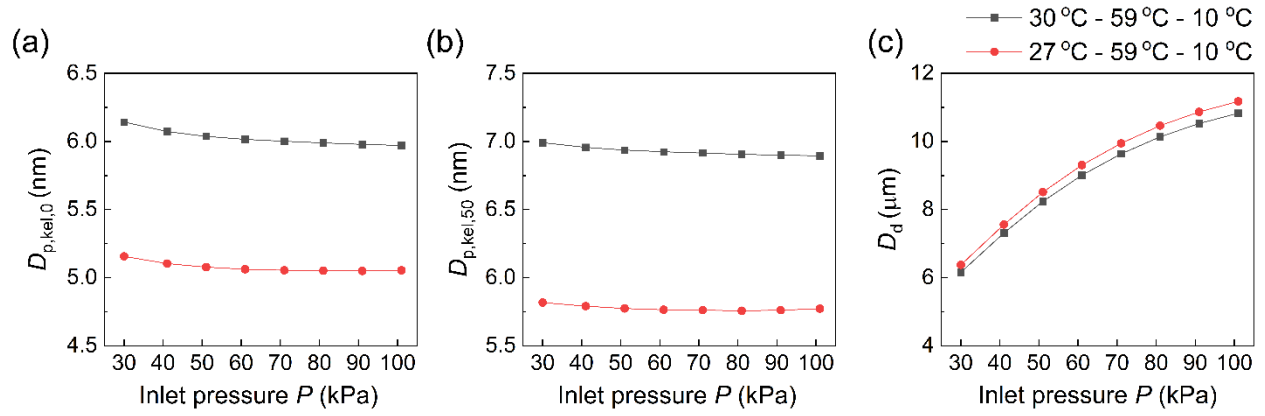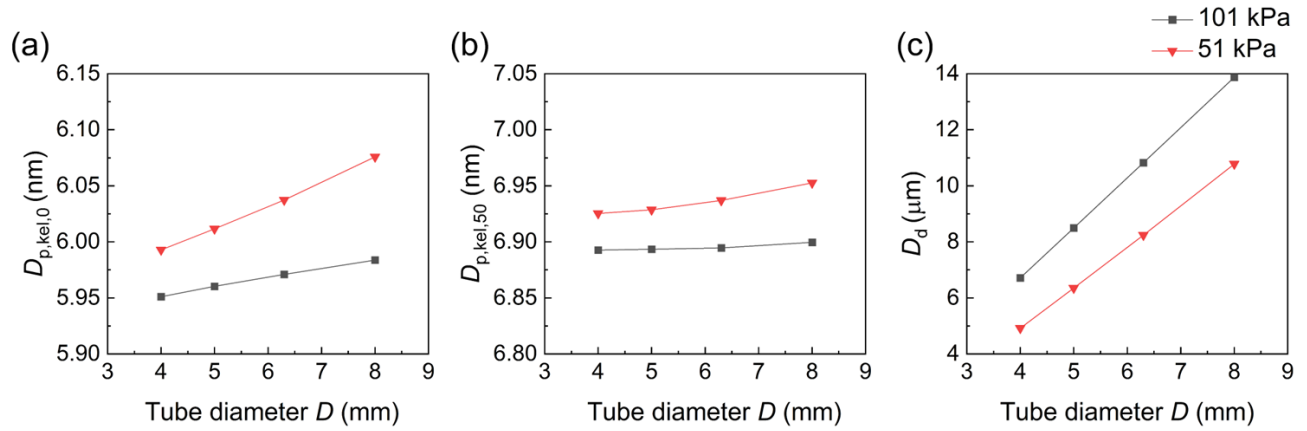
Figure 5. Effect of inlet operation pressure at T_{con}-T_{ini}-T_{mod} of 27−59−10 °C and 30−59−10 °C on (a) minimum activated size, $D_{p,kel,0}$, (b) 50% cut-off size, $D_{p,kel,50}$, and (c) final growth particle size at the outlet of the moderator along the centerline ($r = 0$), D_d. The condensational growth of 8 nm particles was tested as seed particles.

Figure 6. Effect of tube diameter (D) at 51 kPa and 101 kPa on (a) minimum activated size, $D_{p,kel,0}$, (b) 50% cut-off size, $D_{p,kel,50}$, and (c) final growth particle size at the outlet of the moderator along the centerline ($r = 0$), D_d. The condensational growth of 8 nm particles was tested as seed particles.
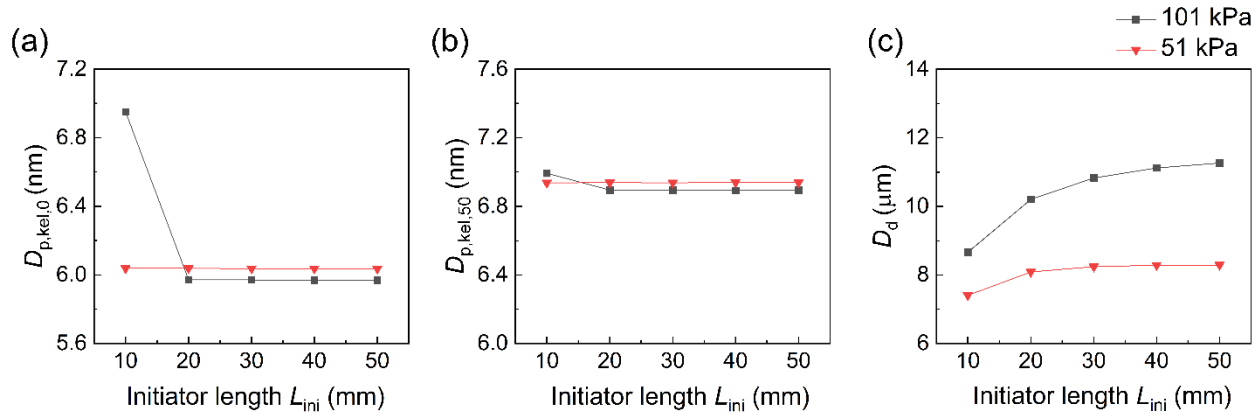
Figure 7. Effect of initiator length (L_{ini}) at 51 kPa and 101 kPa on (a) minimum activated size, $D_{p,kel,0}$, (b) 50% cut-off size, $D_{p,kel,50}$, and (c) final growth particle size at the outlet of the moderator along the centerline ($r = 0$), D_d. The condensational growth of 8 nm particles was tested as seed particles.
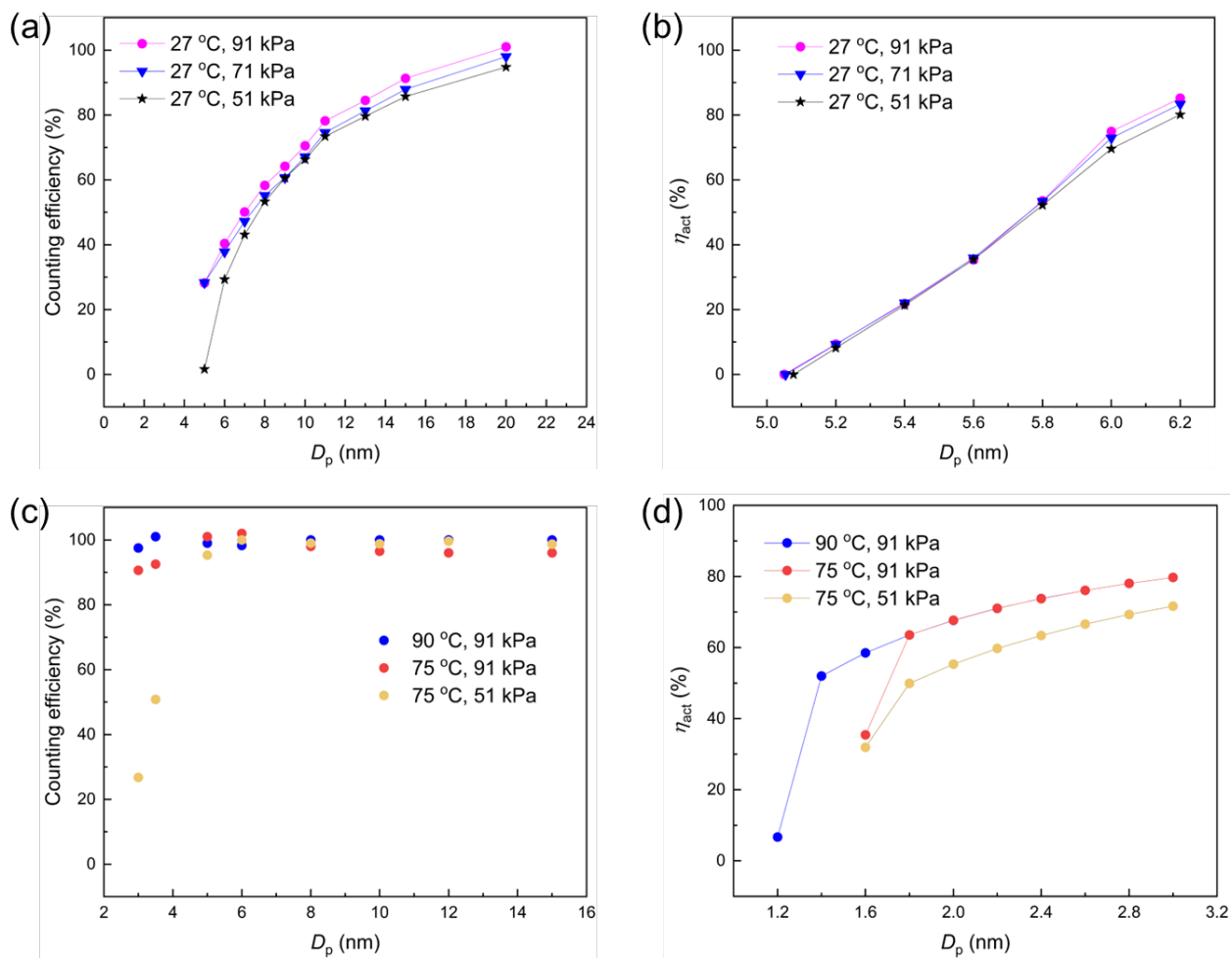
Figure 8. vWCPC operation validation: (a) the counting efficiency of experimental results as a function of particle size under the conditioner temperature of 27 °C and pressure of 91, 71, and 51 kPa for the 7 nm configuration, **(b)** the detection efficiency of simulation results as a function of particle size under the conditioner temperature of 27 °C and pressure of 91, 71, and 51 kPa for the 7 nm configuration, **(c)** the detection efficiency of experimental results as a function of particle size under initiator temperatures of 75 and 90°C and pressure of 91 and 51 kPa for the 2 nm configuration, and **(d)** the detection efficiency of simulation results as a function of particle size under initiator temperatures of 75 and 90°C and pressure of 91 and 51 kPa for the 2 nm configuration.